Available online at BCREC website: https://journal.bcrec.id/index.php/bcrec

Bulletin of Chemical Reaction Engineering & Catalysis, 19 (1) 2024, 15-31

Research Article

Precursor-concentration-controlled Morphology of TiO_2 Nanorod/Nanoflower Films for Enhanced Photoelectrochemical Water Splitting and Investigating Their Growth Mechanism

Sawsan Abdullah Abduljabbar Anaam[1,2,*], Mohd Zainizan Sahdan[3,*]

[1]Microelectronic and Nanotechnology-Shamsuddin Research Centre (MiNT-SRC), Institute of Integrated Engineering, Universiti Tun Hussein Onn Malaysia, 86400 Parit Raja, Johor, Malaysia.
[2]Faculty of Electric and Electronic Engineering, Universiti Tun Hussein Onn Malaysia, 86400 Parit Raja, Johor, Malaysia.
[3]Faculty of Technical Education and Vocational, Universiti Tun Hussein Onn Malaysia, 86400 Parit Raja, Johor, Malaysia.

Received: 24th October 2023; Revised: 7th December 2023; Accepted: 7th December 2023
Available online: 11st December 2023; Published regularly: April 2024

Abstract

Titanium dioxide (TiO_2) has been considered as one of the most promising photocatalysts for photoelectrochemical (PEC) water splitting. Therefore, numerous efforts have been devoted to improving its PEC water splitting performance. In this study, TiO_2 nanorod/nanoflower (NRF) films with controlled morphology were synthesized on fluorine-doped tin oxide (FTO) glass substrates by following a facile one-step hydrothermal method. The TiO_2 NRF films were characterized by X-ray diffraction (XRD), Raman spectroscopy, field emission scanning electron microscopy (FE-SEM), atomic force microscopy (AFM), energy-dispersive X-ray spectrometer (EDS), and ultraviolet-visible (UV-Vis) spectrophotometer. FE-SEM showed that the TiO_2 films are composed of a simultaneous growth of a primary layer of TiO_2 nanorod arrays (NRAs) and a second layer of TiO_2 nanoflowers (NFs). The proposed growth mechanism highlighted the influence of precursor concentration on nucleation sites, affecting the preferred crystallographic plane growth of rutile TiO_2 and nanorod alignment on the FTO substrate. Intriguingly, TiO_2 NRF films prepared with 1.0 mL of titanium butoxide exhibited a maximum photocurrent density of 3.58 $mA.cm^{-2}$ at 1.23 V versus (vs.) the reversible hydrogen electrode (RHE), along with a maximum photoconversion efficiency of 0.69%. The enhanced photocurrent density and photoconversion efficiency were attributed to the optimum thickness in the range of 4.52-7.31 µm, which caused the film to be formed with a unique morphology of the primary layer with well-vertically aligned nanorods and the second layer of flowers consisting of numerous rods stacked on top of one another. This study demonstrates the importance of designing semiconductors with 1D nanorod/3D nanoflower structures as high-performance photoelectrodes for PEC water splitting.

Keywords: TiO_2 1D nanorod/3D nanoflower film; Hydrothermal method; Photoelectrochemical water splitting; Growth mechanism; Photocatalyst

How to Cite: S.A.A. Anaam, M.Z. Sahdan (2024). Precursor-concentration-controlled Morphology of TiO_2 Nanorod/Nanoflower Films for Enhanced Photoelectrochemical Water Splitting and Investigating Their Growth Mechanism. *Bulletin of Chemical Reaction Engineering & Catalysis*, 19(1), 15-31 (doi: 10.9767/bcrec.20061)

Permalink/DOI: https://doi.org/10.9767/bcrec.20061

1. Introduction

The development of renewable energy sources is essential due to the depletion of traditional fossil fuels and the pressure arising from the ongoing energy crisis. Thus, hydrogen is regarded as a major renewable and sustainable energy source to substitute fossil fuel resources. PEC water splitting is being explored as a promising approach for sup-

* Corresponding Author.
Email: zainizan@uthm.edu.my (M.Z. Sahdan);
saanaam22@yahoo.com (S.A.A. Anaam);

plying sustainable and eco-friendly energy [1,2]. TiO_2 has received significant attention as a photocatalyst for PEC water splitting due to its unique properties, such as good physical and chemical stability, low cost, and non-toxicity [3–5]. However, TiO_2 has its own set of drawbacks as a photocatalytic material due to its wide band gap (3.0-3.2 eV) and rapid recombination of photogenerated charge carriers [6–9]. Therefore, various strategies have been used to overcome its drawbacks and enhance its performance in PEC water splitting, including metal and non-metal doping [10–13], heterostructures [14,15], and depositing noble metals [16,17]. Moreover, the morphology of nanostructured TiO_2 materials with different dimensions has been used as one of the most important strategies to enhance their performance in PEC water splitting. TiO_2 nanotube arrays, TiO_2 nanorod arrays, TiO_2 nanostructures, and crystalline core/amorphous shell-structured black TiO_2 nanoparticles were used to improve the PEC performance of TiO_2 [18–21]. However, it is imperative to explore the impact of combining of the 1D (nanorods) and 3D (nanoflowers) dimensions of nanostructured TiO_2 materials on PEC water splitting performance. Since 1D structures provide rapid diffusion for charge carriers in a single direction, resulting in a low recombination rate of photogenerated electron-hole pairs [22]. While 3D nanoflowers improve visible-light harvesting and shorten the transport distance of the photogenerated electron-hole pairs to reach the electrolyte-electrode interface. In addition, the high specific surface area of 3D structures enlarges the contact area with the electrolyte, exposing a lot of active sites for redox reactions [23].

Hydrothermal method is the most convenient and effective method for the fabrication of TiO_2 nanostructures. It is a facile, low-cost, low-temperature, one-step, free-surfactant synthesis method [24]. Numerous studies have synthesized the TiO_2 NRF films by controlling the morphological properties through varying hydrothermal parameters such as reaction temperature, precursor concentration, reaction time, and hydrochloric acid concentration, as well as investigating their performance in dye-sensitized solar cells [25–29]. However, there is a lack of studies concerning the performance of TiO_2 NRF film in PEC water splitting. Therefore, the formation of TiO_2 NRF films with control their morphological properties to improve the PEC water splitting performance needs to be investigated, especially when designing double layers with different dimensional nanostructures. In addition, a detailed investigation of the growth mechanisms is crucial for comprehending how reaction parameters, such as precursor concentration, affect the nucleation sites. This understanding is necessary for designing a film with an ideal alignment of nanorods on the FTO substrate and a unique formation of NFs on TiO_2 NRAs, while also obtaining an optimum thickness of both layers. Consequently, these aspects offer greater potential for enhancing PEC water splitting.

In the current work, the TiO_2 NRF films with morphology and thickness control were synthesized using a facile one-step hydrothermal method. The effect of TiO_2 precursor concentration on the structural, morphological, element-compositional, and optical properties was scrutinized. Furthermore, the growth mechanism of the films was investigated, and it was found that the precursor concentration significantly impacts the nucleation sites, leading to variations in the preferred crystallographic plane growth of rutile TiO_2 and the alignment of the nanorods on the FTO substrate. Furthermore, the PEC properties evaluation shows that there is an optimum precursor concentration for ideal morphology that yields the highest PEC water splitting performance. Additionally, when comparing the TiO_2 NRF films to previous research findings based on morphological modification, our films exhibit notably improved photocurrent density and photoconversion efficiency. Therefore, the integration of 1D (nanorods) and 3D (nanoflowers) dimensions in TiO_2 synthesis, along with the ability to control morphology and thickness, offers a promising approach to address the constraints associated with TiO_2 in PEC water splitting.

2. Materials and Methods

2.1 Materials

Titanium butoxide (TB, $C_{16}H_{36}O_4Ti$, 97%, Sigma Aldrich), Hydrochloric acid fuming (HCl, 37%, Merck), Sodium Sulfate (Na_2SO_4, 99%, Sigma Aldrich), Isopropyl alcohol (IPA, Sys-

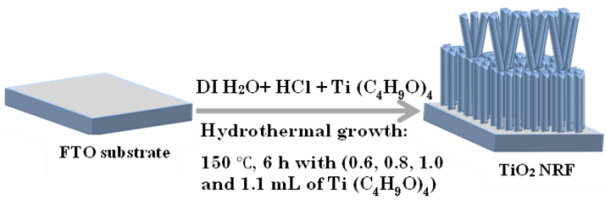

Figure 1. Schematic diagram of hydrothermal synthesis of TiO_2 NRF film with different amounts of TB.

term), and Acetone (Systerm) were used without further purification. FTO substrates (Sigma Aldrich) were cut into pieces of 1.5×2.5 cm^2. The aqueous solutions were prepared with deionized (DI) water.

2.2 Synthesis of TiO_2 NRF Films on FTO Substrate

Figure 1 shows the growth of TiO_2 NRF films on FTO substrates using the one-step hydrothermal method. First, the pieces of FTO substrates were ultrasonically cleaned with acetone, IPA, and DI water, and dried in nitrogen gas flow. TB, HCl, and DI water were used as a TiO_2 precursor, acidic medium, and solvent, respectively. In a typical preparation, 20 mL of HCl was added to 20 mL of DI water and magnetically stirred at room temperature. Afterward, different amounts of TB (0.6, 0.8, 1.0, and 1.1 mL) were added dropwise to the previous solution under continuous stirring. The pieces of FTO substrates were placed horizontally into a 200-mL Teflon-lined stainless-steel autoclave while keeping the FTO-coated side facing up, and then the transparent solution was transferred into it. The autoclave was sealed and heated at 150 °C for 6 h in an electrical oven. Finally, all TiO_2 NRF films were dried for 20 min in the oven and then annealed at 500 °C for 1 h in the oven. These films, which were prepared with 0.6, 0.8, 1.0, and 1.1 mL of TB, are referred to as TiO_2 NRF-0.6, TiO_2 NRF-0.8, TiO_2 NRF-1.0, and TiO_2 NRF-1.1, respectively.

2.3 Characterization

The structural properties of TiO_2 NRF films were analyzed using XRD and Raman spectroscopy. XRD measurements were conducted using a PANalytical X-ray diffractometer with Cu-Kα radiation (wavelength: 1.5406 Å) as the excitation source. The measurements covered Bragg angles from 20° to 80°, and the X-ray tube operated at 40 kV voltage and 40 mA current. The crystallite size (D) was calculated using Scherrer's equation [21,30]:

$$D = \frac{K\lambda}{\beta \cos\theta} \tag{1}$$

where, D is the crystallite size, K is the Scherer constant, λ is the wavelength of the x-ray sources, β is the full-width half-maximum (FWHM), and θ is the peak position (Bragg's diffraction angle). The dislocation density (δ) and microstrain (ε) of the crystal were calculated using Equations (2) and (3), respectively [31,32].

$$\delta = \frac{1}{D^2} \tag{2}$$

$$\varepsilon = \frac{\beta}{4\tan\theta} \tag{3}$$

The lattice parameters were calculated using the equation of tetragonal crystal structure [26].

$$\frac{1}{d^2} = \frac{h^2 + k^2}{a^2} + \frac{l^2}{c^2} \tag{4}$$

Raman spectra of the specimens were carried out using a HORIBA XploRA PLUS Raman system with an excitation laser of 532 nm. The morphological and elemental analyses were characterized by FE-SEM (JOEL, JSM-7600F, Japan, operated at 5 kV in high vacuum) equipped with EDS; Oxford spectrometer, 50 mm2 X-Max silicon drift EDS detector, INCA version of the control software, at an accelerated voltage of 15 kV). AFM (XE-100, Park System) was employed to further examine the morphological properties. The light absorption was recorded on the UV-Vis spectrophotometer (UV-1800 PC model, Shimadzu, Japan). The band gap energy (E_g) was calculated using the following equation:

$$\alpha h\upsilon = A\left(h\upsilon - E_g\right)^n \tag{5}$$

where, α, $h\upsilon$, E_g, and A are the absorption coefficient, photon energy, optical band gap energy, and a constant, respectively. The value of n depends on the electronic transitions (n=1/2 for a direct transition and n=2 for an indirect transition) [33,34].

2.4 PEC Measurements

The PEC measurements were performed using a Solartron 1280C workstation via a typical three-electrode setup. The TiO_2 NRF photoanodes (1.5×1.5 cm^2 area), Pt wire, and Ag/AgCl electrode (3 M NaCl) were employed as the working, counter, and reference electrode, respectively. An aqueous solution of 0.1 M Na_2SO_4 (pH = 7.0) was used as an electrolyte. A 500 W Xe lamp was used as the light source with an incident light intensity of 100 $mW.cm^{-2}$. The linear sweep voltammetry (LSV) measurements were recorded with a scan rate of 10 $mV.s^{-1}$ and a scan range was from −0.6 to 0.8 V vs. Ag/AgCl electrode. The applied potential vs. Ag/AgCl electrode was converted to the RHE scale using the following equation (Equation (6)) [35,36]:

$$E_{RHE} = E_{Ag/AgCl} + E^0_{Ag/AgCl} + 0.059pH \tag{6}$$

where, $E_{Ag/AgCl}$ is the applied potential, $E^0_{Ag/AgCl}$ = 0.209 V for Ag/AgCl reference electrode [3 M NaCl], and pH = 7.0 for Na_2SO_4 electrolyte. Transient photocurrent responses were determined under chopped light irradiation with on/off intervals of 20 seconds (s) at an applied potential of 0.61 V vs. Ag/AgCl electrode. The photoconversion efficiency was evaluated using the following equation:

$$\eta\ (\%) = j_p \left[\frac{\left(E^0_{rev} - \left| E_{app} \right| \right)}{I_0} \right] \times 100 \qquad (7)$$

where, j_p is the photocurrent density (mA/cm^2), E^0_{rev} is the standard reversible potential, which is 1.23 V for water splitting reaction, and the applied potential is $E_{app}=E_{meas}-E_{aoc}$. In the equation, E_{meas} is the electrode potential (vs. Ag/AgCl electrode) of the working electrode at which photocurrent was measured under illumination, and E_{aoc} is the electrode potential (vs. Ag/AgCl electrode) of the same working electrode under open circuit conditions and under the same illumination for the same electrolyte [37].

3. Results and Discussion

3.1 Structural Analysis

XRD was used to investigate the crystalline structure. Figure 2 shows the XRD pattern of TiO_2 NRF-0.6, TiO_2 NRF-0.8, TiO_2 NRF-1.0, and TiO_2 NRF-1.1 samples. The peaks at 2θ = 27.40°, 36.07°, 39.18°, 41.25°, 44.02°, 54.25°, 56.59°, 62.87°, 63.99°, 68.94°, 69.87°, and 76.53°, corresponding to (110), (101), (200), (111), (210), (211), (220), (002), (310), (301), (112), and (202) planes of the TiO_2, respectively, which were also found in the literature [25,38,39]. These diffraction peaks of TiO_2 NRF films are well indexed to the pure rutile phase of the tetragonal crystal structure (JCPD file No: 98-005-1932). The diffraction peaks of the FTO substrate, marked with a star, are indexed to tin oxide (SnO_2) (JCPD file No: 98-005-1932). It can be seen that the diffraction peak (101) of the TiO_2 NRF-0.6 sample has the highest intensity, and this intensity becomes higher for the TiO_2 NRF-0.8 sample. However, when 1.0 mL of TB is added, the intensity of the (101) peak decreases while the intensity of the (110) peak increases. Thus, the (110) peak becomes the prominent peak, and its intensity also increases with the addition of 1.1 mL of TB. The average crystallite sizes were 23.42 nm, 29.53 nm, 29.77 nm, and 26.85 nm for the prepared samples with 0.6 mL, 0.8 mL, 1.0 mL, and 1.1 mL of TB, respectively. The calculated crystallite size, dislocation density, and microstrain of TiO_2 NRF films vary due to the addition of different amounts of TB as given in Table 1. The calculated values of *a* and *c* are

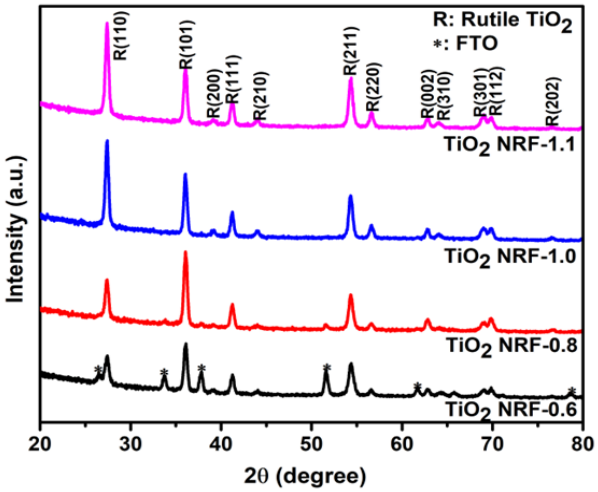

Figure 2. XRD patterns of rutile TiO_2 NRF films prepared with different amounts of TB.

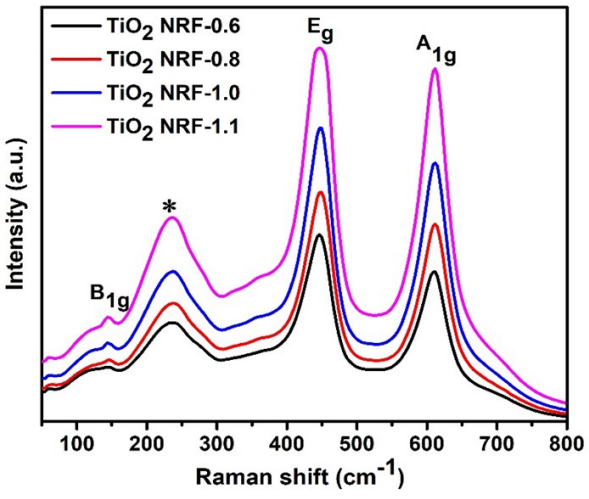

Figure 3. Raman spectra of rutile TiO_2 NRF films prepared with different amounts of TB.

Table 1. Crystallite size (*D*), dislocation density (δ), and microstrain (ε) of TiO_2 NRF films synthesized with different amounts of TB.

Sample	Crystallite size (nm)	δ ×10^{-3} (nm^{-2})	ε ×10^{-3} (line^{-2} m^{-4})
TiO_2 NRF-0.6	23.42	2.70	4.06
TiO_2 NRF-0.8	29.53	1.59	3.07
TiO_2 NRF-1.0	29.77	1.59	3.08
TiO_2 NRF-1.1	26.85	1.72	3.37

4.5980 Å and 2.9564 Å, respectively. These values are in good agreement with the lattice constants a = 4.5980 Å and c = 2.9560 Å of standard data (JCPD 98-005-1932).

Raman spectroscopy serves as a valuable technique for examining the crystallinity and the vibrational structure. Figure 3 displays the Raman spectra of the TiO_2 NRF films which were synthesized with various amounts of TB. Raman peaks at 135 cm^{-1}, 445 cm^{-1}, and 610 cm^{-1} corresponding to the B_{1g}, E_g, and A_{1g} modes of the rutile phase, respectively [40,41]. The two strong bands of E_g and A_{1g} modes originate from O–Ti–O bending vibration and asymmetric Ti–O stretching vibration, respectively. The weak band of B_{1g} is attributed to the rotation of the TiO_6 octahedra around the c-axis [40,42]. The broad peak at 236 cm^{-1} (marked with a star) is a distinctive feature of the rutile phase arising from the second-order scattering or disorder effects [43,44]. The Raman peaks are consistent with XRD peaks which show the presence of the rutile phase of TiO_2. It can be seen that the intensities of the peaks increase as the TB amounts increase, resulting in an enhancement in crystallinity. This increase in intensity was reported in the literature [45]. In addition, the I_{A1g}/I_{Eg} intensity ratios for the films prepared with 0.6 mL, 0.8 mL, 1.0 mL, and 1.1 mL of TB were 0.84, 0.88, 0.90, and 0.93, respectively. These ratios also indicate an improvement in crystallinity [41]. This analysis was supported by the result of the XRD characterization in Figure 2, which shows that the intensity of the prominent peak (110) increases as the TB amount increases.

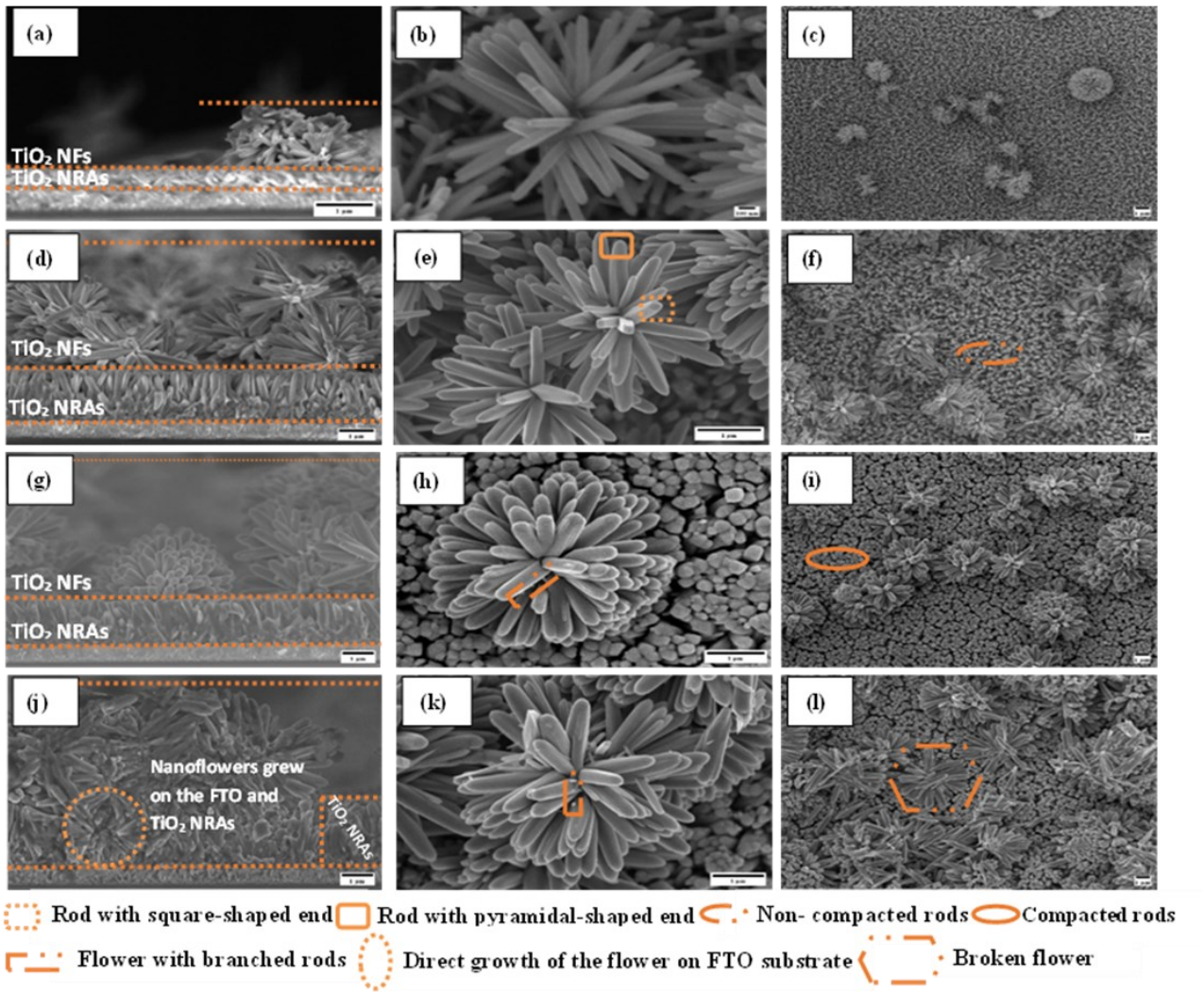

Figure 4. FESEM images of rutile TiO_2 NRF films prepared with different amounts of TB: (a) cross section and (b & c) top view of TiO_2 NRF-0.6; (d) cross section and (e & f) top view of TiO_2 NRF-0.8; (g) cross section and (h & i) top view of TiO_2 NRF-1.0; (j) cross section and (k & l) top view of TiO_2 NRF-1.1.

3.2 Morphological Analysis and Growth Mechanism

The cross-sectional and top-view images of the produced samples were examined using FESEM. The cross-section images (Figure 4(a), (d), (g), and (j)) display that the TiO_2 NRF films consist of two layers: a primary layer of 1D TiO_2 NRAs and a second layer of 3D TiO_2 NFs. The successful growth of TiO_2 1D nanorod/3D nanoflower on the FTO substrates can be explained by the following reactions [46]:

Hydrolysis:

$$Ti(OC_4H_9)_4 + 4H_2O \rightarrow Ti(OH)_4 + C_4H_9OH \quad (8)$$

Condensation:

$$Ti(OH)_4 \rightarrow TiO_2 + 2H_2O \quad (9)$$

Initially, the hydrolysis process occurs when titanium butoxide reacts with water, forming $Ti(OH)_4$ and C_4H_9OH by replacing the ($OC_4H_9^-$) group of TB with the (OH^-) group of H_2O. Ti^{4+} in $Ti(OH)_4$ has the d2sp3 hybridization, involving six hybrid orbitals. Four of these orbitals are occupied by OH ligands. While the remaining two orbitals are occupied by H_2O (aquo ligand) in aqueous solutions, resulting in the formation of a neutral octahedral hydroxo-aquo complex $[Ti(OH)_4(OH_2)_2]^0$ [47].

However, these neutral complexes aggregate and produce non-crystalline TiO_2 because of the spontaneous condensation, and there is no repulsion force involved. The addition of HCl reduces the concentration of OH groups and protonates OH ligands, which leads to the formation of positively charged complexes and, thereby, increases electrostatic repulsion while preventing immediate condensation [48]. At room temperature, the positively charged complexes repel one another due to the electrostatic repulsion. While at the reaction temperature, the complexes gain kinetic energy, which is required to overcome the repulsion and aid in complexes aggregation through the condensation process, which occurs in two stages. The first stage involves the removal of H_2O ligands through an olation process, which results in octahedral chains. The next stage is oxolation, which replaces the remaining OH ligands with oxo-bridges and joins the chains together to form 1D nanorod/3D nanoflower of TiO_2. When higher positive charged complexes participate in condensation, they will be naturally repelled into a more stable linear edge-shared linking, which is a feature of rutile [49].

The growth of 1D NRAs of TiO_2 (primary layer) on the FTO substrate can be justified by considering the nucleation sites on the FTO. When 0.6 mL of TB is used to prepare TiO_2, the rods start to grow on the surface of the FTO substrate in a random alignment (Figure 4(a)), while in the presence of 0.8 mL of TB, denser and thicker nanorods are formed with less randomly aligned rods (Figure 4(d)). With the further increase of the TB to 1.0 mL, the rods are well-aligned and vertically grown on the FTO substrate (Figure 4(g)). By increasing the titanium amount to 1.1 mL, some of the rods align vertically on the FTO substrate, and some of them disappear because of the direct growth of some nanoflowers on the FTO substrate (Figure 4(j)). In addition, it can be observed that as the amount of TB gradually increases, the length of TiO_2 NRAs, and thickness of TiO_2 NFs increase, as summarized in Table 2. The TiO_2 NRF films grow on the FTO substrate without using surfactants or templates. This is because the FTO substrate and TiO_2 have the same crystal structures; they have tetragonal rutile structures, and there is only 2% of a lattice mismatch between FTO ($a = b = 0.4687$ nm) and TiO_2 ($a = b = 0.4593$ nm). Thus, the epitaxial nucleation and growth of the rutile TiO_2 nanorods on the FTO substrate can be promoted by this slight lattice mismatch [50]. It is reported that the molecules on the FTO substrate act as nucleation sites for TiO_2 NRAs growth on the FTO substrate [51]. The change in the growth of the nanorods on the FTO substrate can be attributed to the effect of TB amount on the nucleation sites of the TiO_2. The plentiful supplies of titanium precursor promote the nucleation sites of TiO_2. A few nucleation sites form rods with random alignments because of the large space between the rods, whereas numerous nucleation sites form rods with vertical growth and leave no space for

Table 2. Diameter, length, and thickness of TiO_2 NRF films synthesized with different amounts of TB.

Sample	Rod diameter of TiO_2 NRF film (μm)	Length of TiO_2 NRAs (μm)	Thickness of TiO_2 NFs (μm)	Thickness of TiO_2 NRF film (μm)
TiO_2 NRF-0.6	0.06-0.08	0.48	1.16-1.38	1.64-1.86
TiO_2 NRF-0.8	0.15-0.19	1.73	1.85-4.23	3.58-5.96
TiO_2 NRF-1.0	0.20-0.25	1.81	2.71-5.50	4.52-7.31
TiO_2 NRF-1.1	0.25-0.30	2.65	2.86-6.92	5.51-9.57

random growth [52]. Cl^- of HCl plays a significant role in the growth of TiO_2 grains into nanorods. This is due to the preferential adsorption of Cl^- on the surface of the {110} planes, which have a positive polar face. This preferential adsorption of Cl^- prevents TiO_2 grains from contacting the surface of the {110} planes, which consequently accelerates the growth along the {001} plane. As a result, the growth of TiO_2 grains can be suppressed in the [110] direction and accelerated in the [001] direction, which leads to the formation of rod structures [53].

The growth of 3D NFs of TiO_2 (the second layer) on the TiO_2 NRAs (the primary layer), can be justified by considering the rods of the primary layer, which are greatly impacted by the nucleation sites on the FTO substrate. TiO_2 NRAs have a square-shaped end and a pyramidal-shaped end (top-view image in Figure 4(e)). Therefore, it can be indicated that the pyramidal-shaped and square-shaped ends of the TiO_2 NRAs may serve as nucleation sites for the TiO_2 NFs growth over the TiO_2 NRAs. It is reported that the pyramidal-shaped ends of the TiO_2 NRAs act as nucleation sites for the TiO_2 NFs growth [51,54]. When the nucleation sites (the rods of the primary layer) are few, the flowers of the samples that were prepared with 0.6 mL and 0.8 mL of TB consist of few rods that are not compacted or closed to each other in the center of the flowers (Figure 4(b) and (e)). The main difference between them is that the rod diameters of the flowers of the TiO_2 NRF-0.8 sample are larger than those of the TiO_2 NRF-0.6 sample as shown in Table 2. After the addition of 1.0 mL of TB, it was observed that the individual flower is influenced by a large number of nucleation sites. The rods become close to each other in the center of the flower, and branched rods start to be formed (Figure 4(h)). In addition, the flower becomes thicker because it forms from many rods that are stacked on top of each other [55]. By adding 1.1 mL of TB, the individual flower becomes thicker with more branched nanorods com-

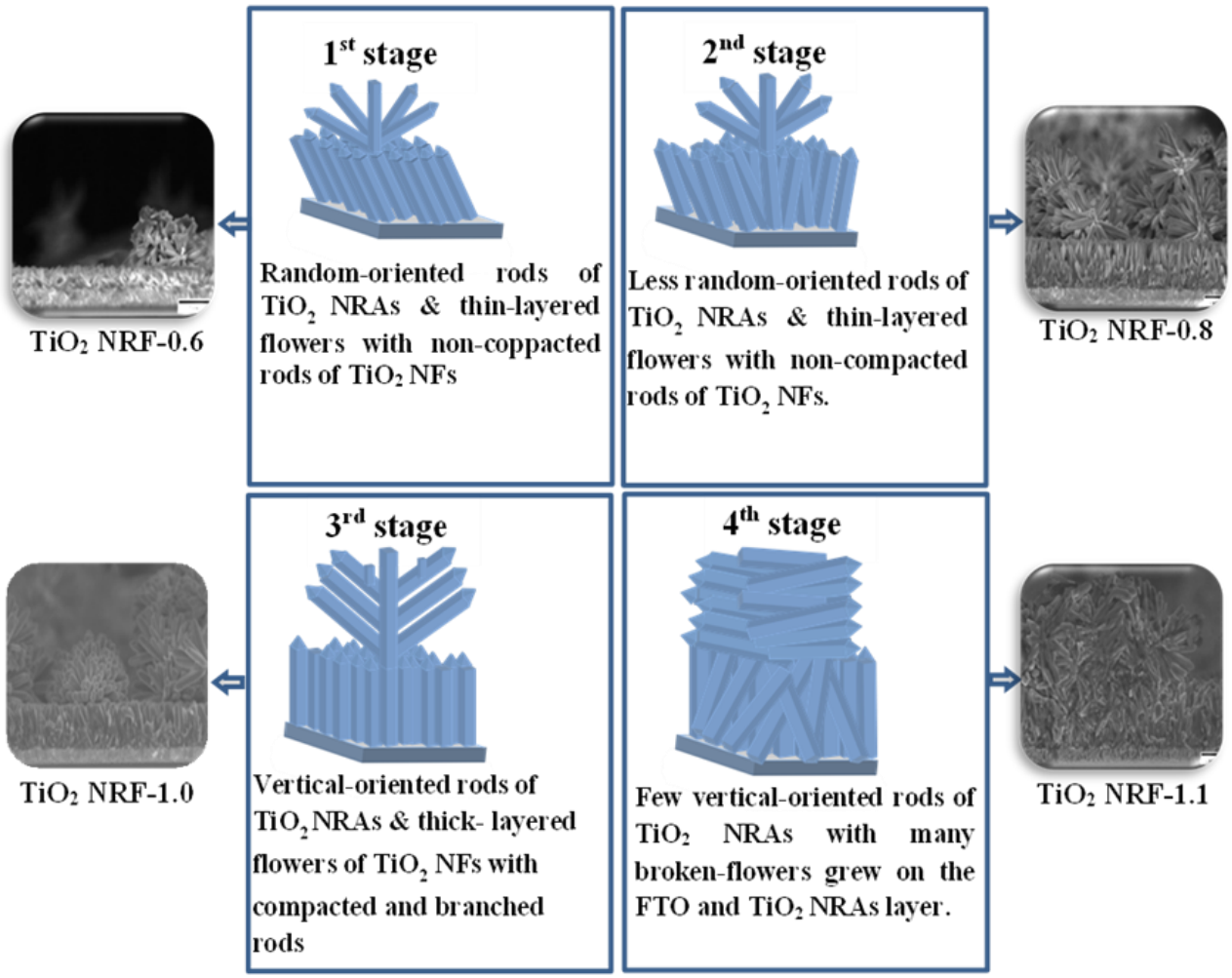

Figure 5. Schematic diagram for the proposed growth model of TiO_2 NRF films prepared with different amounts of TB.

pared to the TiO_2 NRFFs-1.0 sample (Figure 4(k)). The top-view images (Figure 4(c), (f), (i), and (l)) display the growth of many nanoflowers above the primary layer (1D TiO_2 NRAs). It can be observed that as the TB amount increases, the thicknesses of both layers increase. However, by adding 1.1 mL of TB, some flowers are broken and consist of separated rods that have horizontal alignment due to the high nucleation density [56]. These results suggest that the preferred crystallographic plane growth of the rutile TiO_2 and the alignment of the nanorods on the FTO substrate are affected by the nucleation sites, which are highly influenced by the TB amount.

Based on the above growth mechanism, a model for the prepared samples with different amounts of TB is proposed (Figure 5). To provide this model, we focused on the rod alignment of TiO_2 NRAs, the formation of TiO_2 NFs, the shapes of rods in the TiO_2 NRAs and TiO_2 NFs layers, as well as the gradual increase in the diameter and length of the nanorods and the thickness of the nanoflowers. This proposed growth model consists of four stages. The first stage is proposed for the samples that were prepared with 0.6 mL of TB. The TiO_2 NRF films are formed with random-oriented rods of TiO_2 NRAs and with thin-layered flowers with non-compacted rods of TiO_2 NFs (Figure 5, 1st stage). The second stage is proposed for the samples that were prepared with 0.8 mL of TB. The TiO_2 NRF films are formed with less random-oriented rods of TiO_2 NRAs and thin-layered flowers with non-compacted rods of TiO_2 NFs (Figure 5, 2nd stage). The third stage is proposed for the samples that were prepared with 1.0 mL of TB. The NRF films formed with vertical-oriented rods of TiO_2 NRAs and thick-layered flowers of TiO_2 NFs with compacted and branched rods (Figure 5, 3rd stage). The fourth stage is proposed for the samples that were prepared with 1.1 mL of TB. The TiO_2 NRF films are formed with few vertically oriented rods of TiO_2 NRAs with many broken flowers growing on the FTO substrate or on the TiO_2 NRAs layer (Figure 5, 4th stage).

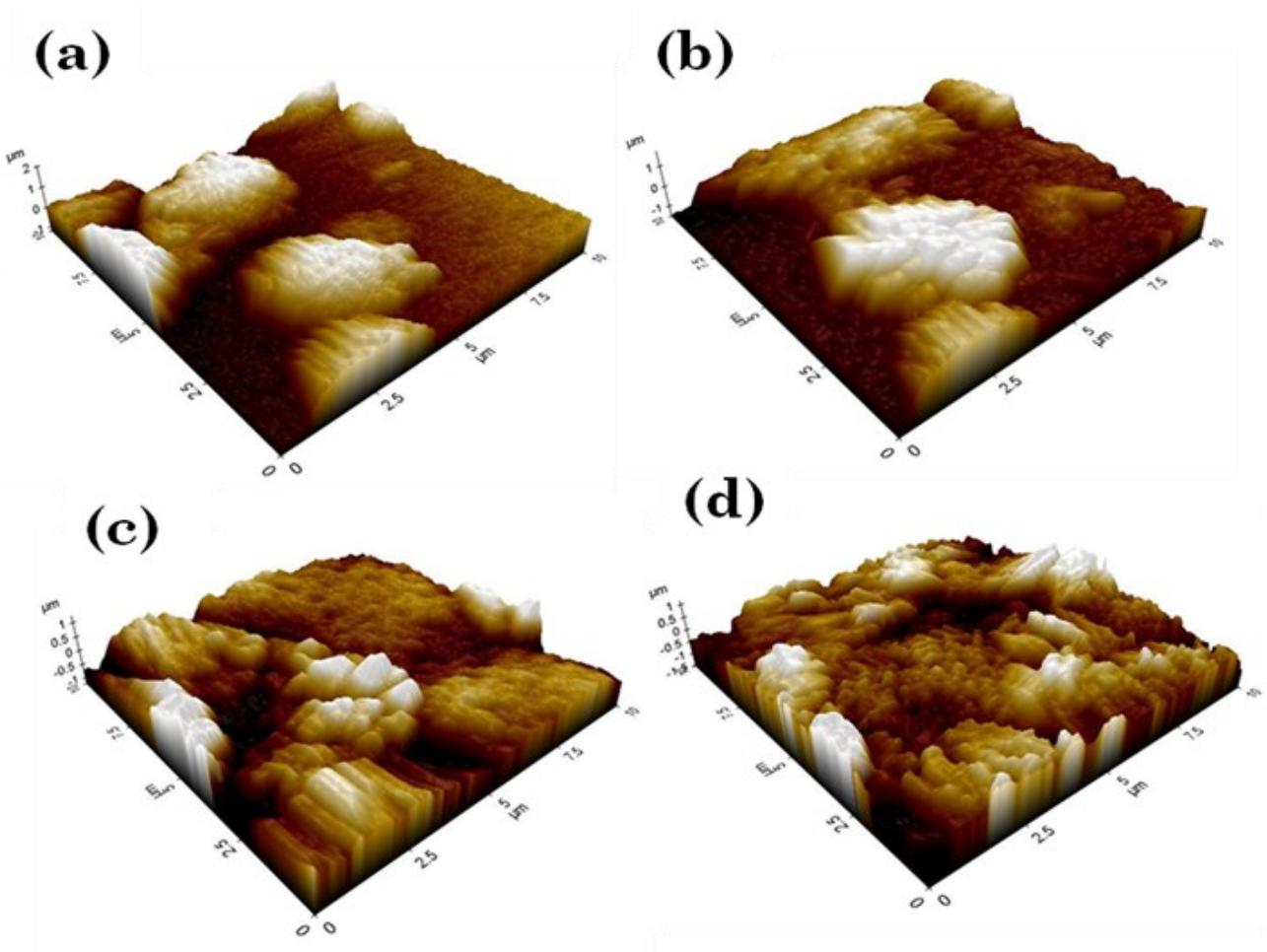

Figure 6. AFM images of rutile TiO_2 NRF films prepared with different amounts of TB: (a) TiO_2 NRF-0.6, (b) TiO_2 NRF-0.8, (c) TiO_2 NRF-1.0, and (d) TiO_2 NRF-1.1.

The AFM topography images of the TiO_2 NRF films prepared with different amounts of TB are shown in Figure 6. The TiO_2 NRF films, produced using 0.6 mL, 0.8 mL, 1.0 mL, and 1.1 mL, exhibit root-mean-square (RMS) roughness values of 0.578 µm, 0.614 µm, 0.300 µm, and 0.336 µm, respectively. The addition of 1.0 mL of Tb results in the lowest RMS roughness value. The morphological analysis using FE-SEM and AFM reveals that samples prepared with 1.0 mL of TB exhibit the formation of TiO_2 nanorods arranged vertically and thick-layered TiO_2 nanoflowers with compacted and branched rods. Additionally, these samples display the lowest RMS roughness value.

3.3 Elemental Composition Analysis

EDS was used to identify the elemental composition of the TiO_2 NRF films prepared with various amounts of TB. Titanium (Ti) and oxygen (O) are present in all prepared samples, which confirms that Ti and O are the elemental components of TiO_2 NRF films (Figure 7(a), (b), (c), (d)). Compared to the TiO_2 NRF-0.6 sample, Peaks of the TiO_2 NRF-0.8, TiO_2 NRF-1.0, and TiO_2 NRF-1.1 samples at 4.51 eV and 0.52 eV are prominent. The additional peak of C is caused by carbon tape [57], and the peak of Si in the TiO_2 NRF-0.6 sample comes from the EDS detector. Table 3 summarized the atomic percentages of the elements found in the characterized TiO_2 NRF films.

3.4 Optical Properties

Figure 8 shows the absorption spectra of the TiO_2 NRF films prepared with various amounts of TB. The absorption band edge of the samples is in the range of 400-420 nm, as

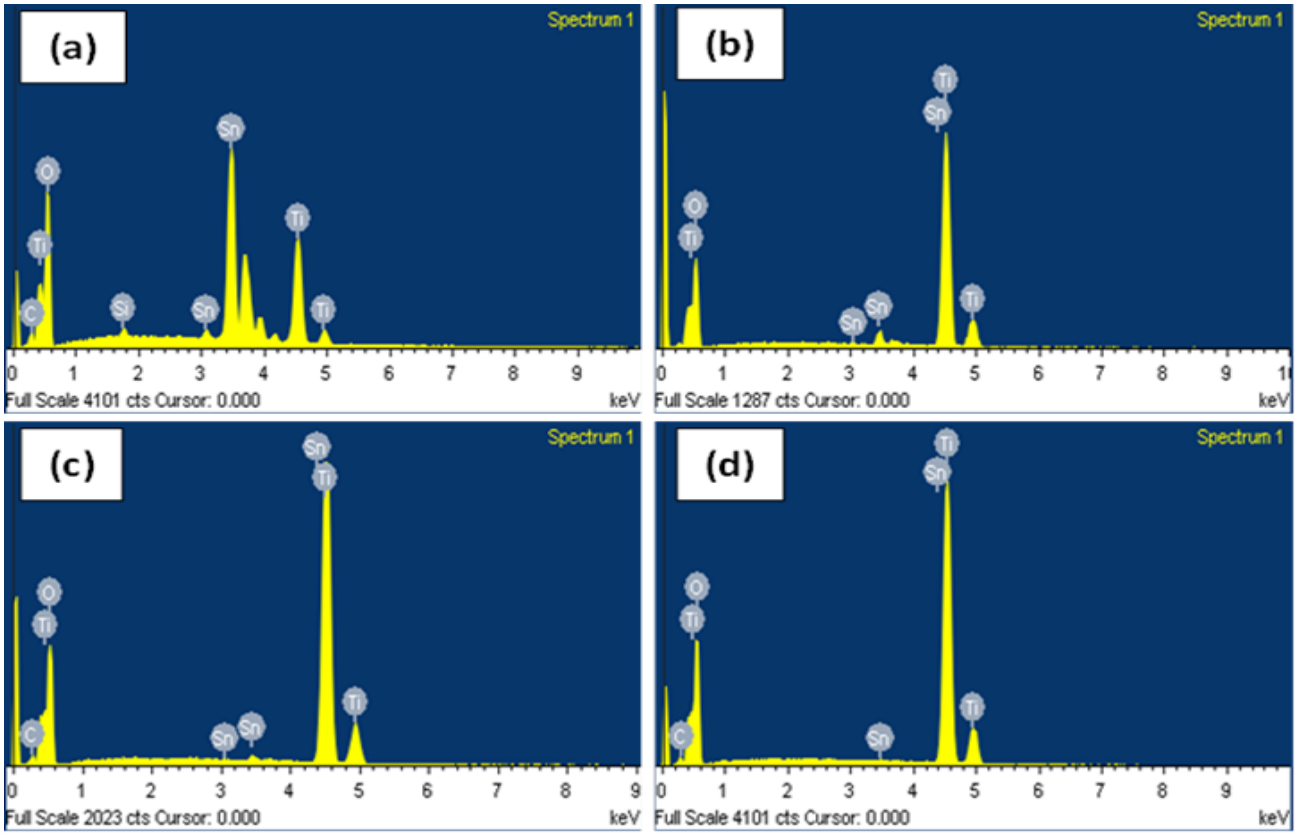

Figure 7. EDS of rutile TiO_2 NRF films prepared with different amounts of TB: (a) TiO_2 NRF-0.6, (b) TiO_2 NRF-0.8, (c) TiO_2 NRF-1.0, and (d) TiO_2 NRF-1.1.

Table 3. Atomic percentages of the elements found in the characterized TiO_2 NRF films from the EDS analysis.

Sample	O	Ti	Sn	C	Si
TiO_2 NRF-0.6	76.09	10.02	10.54	3.00	0.34
TiO_2 NRF-0.8	70.37	28.59	1.04	-	-
TiO_2 NRF-1.0	68.14	28.43	0.3	3.13	-
TiO_2 NRF-1.1	69.53	27.41	0.15	2.91	-

shown in Figure 8(a). The same range of the absorption band edge has been found in literature [58]. The samples exhibit enhanced absorption when the amount of TB increases. It can be observed that the TiO_2 NRF film, produced using 0.6 mL of TB, exhibits strong absorption in the visible light spectrum in the range of 406–532 nm. This phenomenon can be ascribed to the limited coverage of the TiO_2 NRF film on the FTO substrate surface and the

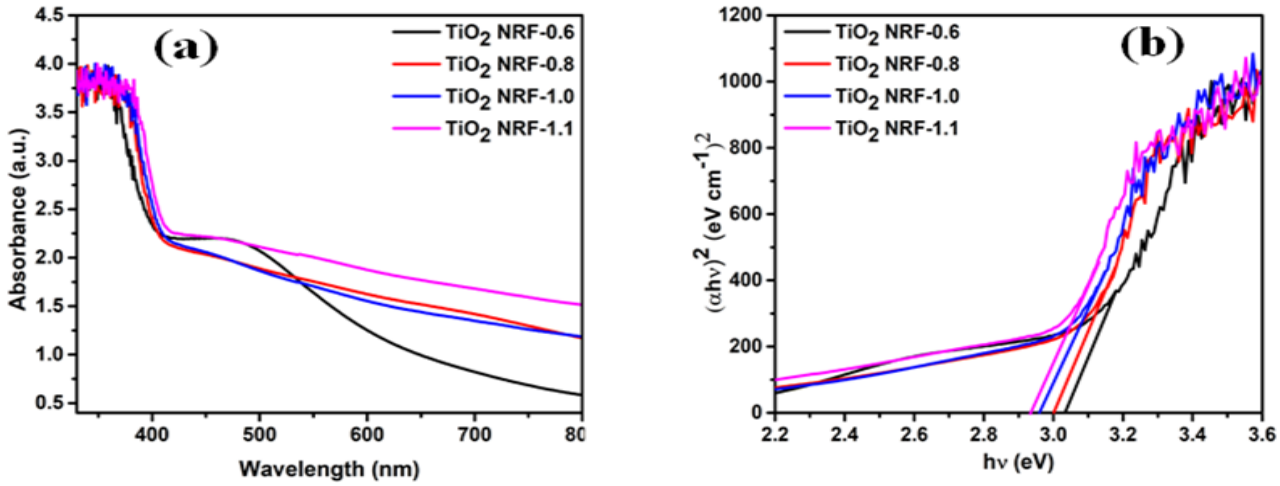

Figure 8. (a) Optical absorption spectra and (b) band gap of rutile TiO_2 NRF films prepared with different amounts of BT.

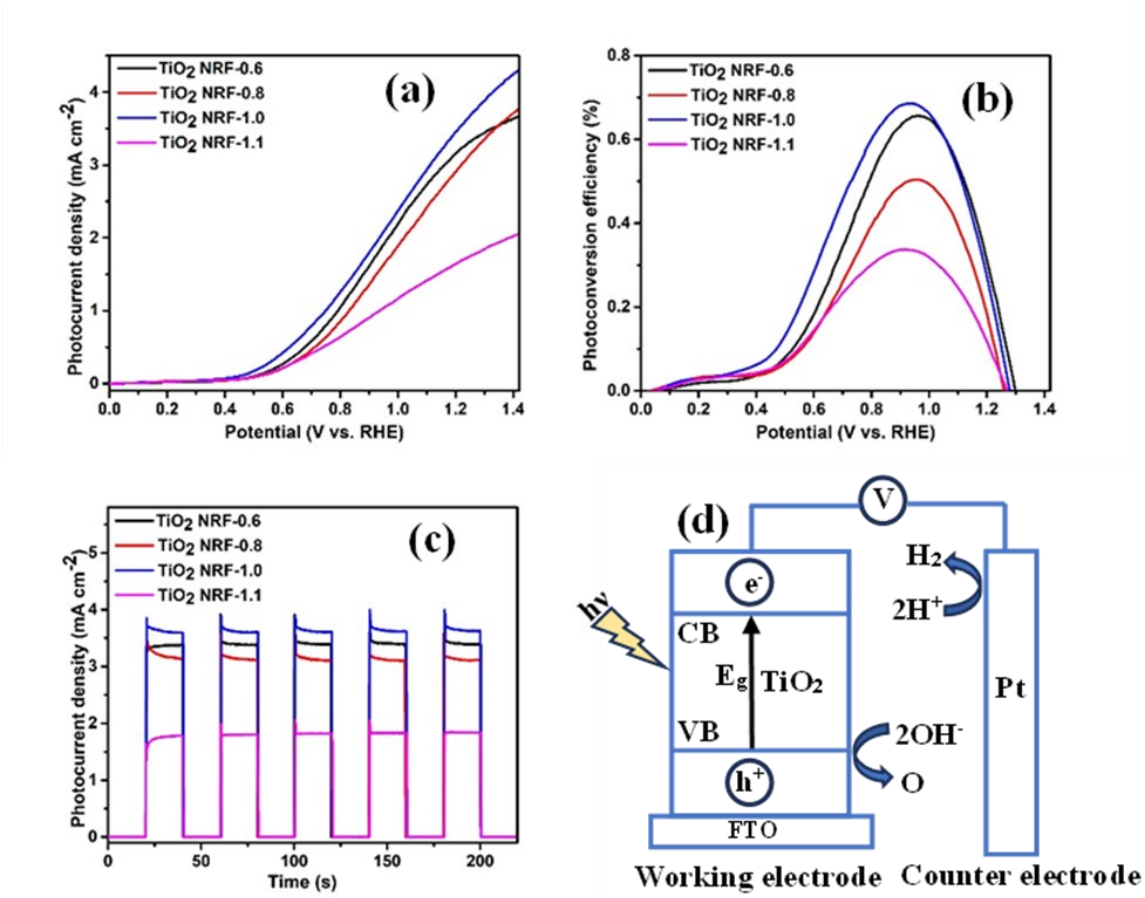

Figure 9. PEC performance of rutile TiO_2 NRF films: (a) Photocurrent–potential (J–V) curves, (b) photoconversion efficiency, (c) photocurrent density vs time, and (d) schematic diagram for the proposed mechanism of the PEC water splitting process.

abundance of Sn. This can be observed from the XRD analysis, indicating multiple peaks associated with SnO_2 from the FTO substrate. Additionally, the EDS results indicate a higher atomic percentage of Sn (10.54%) compared to Ti (10.02%). Indeed, FTO possesses high optical transparency within the visible spectrum [59].

The band gap energies were determined by extrapolating the tangent line of the $(\alpha h\nu)^2$ plot drown vs. ($h\nu$) (Figure 8(b)). The calculated band gap energy values for samples prepared with 0.6 mL, 0.8 mL, 1.0 mL, and 1.1 mL of TB are 3.04 eV, 3.00 eV, 2.96 eV, and 2.94 eV, respectively. These results suggest that as the amount of TB increases, there is a corresponding decrease in the band gap energy. These optical properties indicate that the large specific surface area of nanoflowers causes the light to be scattered in all directions and to be multiply absorbed. Therefore, the nanoflower structures boost the light-harvesting ability, this enhancement of nanoflower structures for the light-harvesting ability was observed in the literature [60,61].

3.5 PEC Performance

To evaluate the PEC water splitting performance of the films which were synthesized with different TB amounts, linear sweeping voltammetry (LSV), photoconversion efficiency, and transient photocurrent response were conducted. Figure 9(a) shows the photocurrent density-potential (J-V) curves of the TiO_2 NRF films obtained by linear sweep voltammetry measurements using a three-electrode electrochemical system in 0.1 Na_2SO_4 electrolyte under 100 mW.cm^{-2} (AM 1.5G) illumination. The photocurrent densities of the TiO_2 NRF-0.6, TiO_2 NRF-0.8, TiO_2 NRF-1.0, and TiO_2 NRF-1.1 are 3.25, 3.04, 3.58, and 1.70 mA.cm^{-2} at 1.23 V vs. RHE, respectively. The TiO_2 NRF-1.0 film shows the highest photocurrent density. This can be credited to the unique morphology of the film, which formed with the TiO_2 NRAs layer composed of well-vertically aligned nanorods and TiO_2 NFs layer consisted of numerous rods placed on top of one another on the side of the flower and closed to one another in the center. The enhanced photocurrent density can also be attributed to the lowest roughness value. Ramli et al. found that the optimal thickness and lowest RMS roughness value enhanced the photocurrent density [62]. However, the TiO_2 NRF-1.1 film exhibits a lower value of photocurrent density even though it has greater absorption and a narrower band gap compared to the TiO_2 NRF-1.0 film. This may suggest that the formation of the horizontally aligned nanorods of the second layer (broken nanoflowers) on the surface of the vertically aligned nanorods of the primary layer creates an intersection of the nanorods of both layers, providing spots for electron-hole recombination and significantly hampering the transport of charge carriers, thereby reducing the activity of the photocatalyst [20]. Moreover, the TiO_2 NRF-0.6 film exhibits a higher photocurrent density value than the TiO_2 NRF-0.8 film. This difference can be attributed to the higher atomic percentages of Sn in the TiO_2 NRF-0.6 film compared to the TiO_2 NRF-0.8 film samples, leading to an increase in absorption within the visible light spectrum in the range of 406–532 nm and enhancing electron mobility [63,64]. Figure 9(b) shows the photoconversion efficiency of the TiO_2 NRF films. The efficiencies for the samples synthesized with 0.6 mL, 0.8 mL, 1.0 mL, and 1.1 mL of TB are 0.66% at a bias of 0.95 V vs. RHE, 0.50% at a bias of 0.95 V vs. RHE, 0.69% at a bias of 0.94 V vs. RHE, and 0.34% at a bias of 0.92 V vs. RHE, respectively. The maximum efficiency is seen for the TiO_2 NRF-1.0 film, which is 1.05 times higher than the TiO_2 NRF-0.6 film, 1.38 times higher than the TiO_2 NRF-0.8 film, and even 2.03 times higher than the TiO_2 NRF-1.1 film. Table 4 summarizes the photocurrent density and photoconversion efficiency of the prepared films of TiO_2 NRF.

The transient current response studies were conducted to further evaluate the performance of the prepared TiO_2 films under visible light. The transient photocurrent response was

Table 4. Photocurrent density and photoconversion efficiency of TiO_2 NRF films prepared with different amount of TB.

Sample	Photocurrent density (mA.cm^{-2})	Photoconversion efficiency (%)
TiO_2 NRF-0.6	3.25	0.66
TiO_2 NRF-0.8	3.04	0.50
TiO_2 NRF-1.0	3.58	0.69
TiO_2 NRF-1.1	1.70	0.34

measured at a potential of 0.61 vs. Ag/AgCl electrode (1.23 V vs. RHE). It can be observed from Figure 9(c) that the photocurrent remains constant as long as the light is turned on, while it drops to zero when the light is turned off. The current is generated by electron-hole pair separation at the semiconductor-electrolyte interface. The holes are trapped by the reduced species in the electrolyte, while the electrons are transported to the cathode via the TiO_2 NRF films and the conductive layer of the FTO glass substrate [65,66]. All samples display fast photo-response under alternating light-on and light-off conditions, and the photocurrent is highly reproducible for numerous on-off illumination cycles. This can be attributed to good crystallinity and good contact between the films and the FTO substrate.

The proposed mechanism for the PEC water splitting of the TiO_2 NRF film is shown in Figure 9(d). The photoanode (TiO_2 NRF film) and cathode (Pt wire) were immersed in the electrolyte and connected via the externally applied potential. When the TiO_2 NRF film is exposed to visible light, electrons in the valence band (VB) are excited to the conduction band (CB), and holes are left in the VB. These photogenerated electron-hole pairs are separated by the applied potential. The holes in the valence band oxidize the water to produce oxygen, while the electrons move to the cathode to produce hydrogen [67]. The TiO_2 NRF-1.0 film shows the highest photocurrent density and photoconversion efficiency due to its unique morphology and roughness. a comparison of the PEC performance with values from the literature is displayed in Table 5, which is conducted based on the morphological modification. It can be clearly seen that the TiO_2 NRF films provide considerably improved photocurrent density and photoconversion efficiency as compared to those reported in the literature.

4. Conclusion

The TiO_2 NRF films grown on FTO substrates are obtained using the hydrothermal method. FE-SEM shows that the TiO_2 NRF films are composed of the simultaneous growth of two layers: a primary layer of TiO_2 NRAs

Table 5. Comparison of photocurrent density and photoconversion for TiO_2 based on the morphological modification.

Photoanode	Light source	Electrolyte	Photocurrent density	Efficiency	Refs.
TiO_2 nanorod arrays	500 W Xe lamp	0.5 M Na_2SO_4	0.27 mA.cm^{-2} vs. Ag/AgCl electrode	0.089% at 0.7 V vs. RHE	[19]
TiO_2 nanorod arrays	UV–vis light	0.1 M Na_2SO_3	4 mA.cm^{-2} at 0.2 V vs. Ag/AgCl electrode	-	[68]
TiO_2-rutile/anatase homojunction	150 W Xe lamp	0.5 M Na_2SO_4	1.70 mA.cm^{-2} at 0.6 V vs. SCE*	0.30% at 0.25 V vs. SCE	[69]
Core/amorphous shell structured TiO_2 NPs	Visible light	1.0 M NaOH	0.20 mA.cm^{-2} at 0 V vs. Ag/AgCl electrode	0.147% at 0.45 V vs. RHE	[21]
TiO_2 nanostructures	150 W Xe lamp	0.5 M NaOH	149.1 μA.cm^{-2} at 0.8 V vs. Ag/AgCl electrode	-	[20]
Porous TiO_2 hollow hemispheres	solar simulator	1.0 M KOH	0.71 mA.cm^{-2} at 1.23 V vs. RHE	0.27%	[70]
TiO_2 nanotube array	Xe lamp	1.0 M NaOH	1.13 mA.cm^{-2} at 1.23 V Vs. RHE	0.957% at 0.324 V vs. RHE	[18]
Reduced TiO_2 nanotubes	solar simulator	1.0 M KOH	126.89 μA.cm^{-2} at 1.23 vs. RHE	0.083%	[71]
TiO_2 NRF-1.0	500 W Xe lamp	0.1 M Na_2SO_4	3.58 mA.cm^{-2} at 1.23 vs. RHE	0.69 at 0.94 V vs RHE	This work

that grew on the FTO substrate and a second layer of TiO_2 NFs that grew on the primary layer of 1D TiO_2 nanorod arrays. The proposed growth mechanism of both layers of the TiO_2 NRF films showed that the precursor amount affects the nucleation sites, which has a significant impact on the preferred crystallographic plane growth of rutile TiO_2 and the nanorods alignment on the FTO substrate. Moreover, the TiO_2 NRF films displayed the highest photocurrent density and photoconversion efficiency, measuring 3.58 $mA.cm^{-2}$ (at 1.23 V vs. RHE) and 0.69%, respectively. The finding revealed that by optimizing the titanium butoxide amount to 1.0 mL, the TiO_2 NRF films are obtained with a special thickness in the range of 4.52-7.31 μm, which formed a distinct morphology. This film is composed of the TiO_2 NRAs layer with perfectly vertically aligned nanorods and the TiO_2 NFs layer with numerous rods layered on top of one another on the side of the flower and closed to one another in the center. Additionally, the film exhibited the lowest root mean square (RMS) value of 0.300 μm. It can be concluded that the synthesis of TiO_2 NRF films with the ideal thickness, unique two-layer formation, and low RMS roughness value are desirable characteristics for TiO_2 NRF film to improve its PEC water splitting performance. Our study demonstrates that the facile one-step hydrothermal process, when carefully adjusting the precursor concentration to achieve the optimum morphology, can be applied not only to produce an ideal TiO_2 NRF film but also can be readily employed with a diverse range of other semiconductor materials to enhance the efficiency of converting solar energy into chemical energy.

Acknowledgment

The authors would like to thank the Microelectronics and Nanotechnology Shamsuddin Research Centre (MiNT-SRC) at Universiti Tun Hussein Onn Malaysia (UTHM) for allowing us to use the UV-Vis spectrophotometer, and Solartron 1280C workstation. The authors also thank Mrs. Faezahana Mohkhter for her assistance with XRD, Raman spectroscopy, and AFM tests, as well as Mr. Ahmad Nasrull for his assistance with FE-SEM imaging and EDS.

CRediT Author Statement

S.A.A. Anaam: Conceptualization, Methodology, Investigation, Data Curation, Formal Analysis, Writing-original draft; *M.Z. Sahdan*: Resources, Review and Editing, Supervision. All authors have read and agreed to the published version of the manuscript.

References

[1] Jiang, L., Li, H., Mu, J., Ji, Z. (2018). Manipulation of surface plasmon resonance of sputtered gold-nanoparticles on TiO_2 nanostructured films for enhanced photoelectrochemical water splitting efficiency. *Thin Solid Films*, 661, 32–39. DOI: 10.1016/j.tsf.2018.07.010.

[2] Li, Z., Shi, L., Franklin, D., Koul, S., Kushima, A., Yang, Y. (2018). Drastic enhancement of photoelectrochemical water splitting performance over plasmonic Al@TiO_2 heterostructured nanocavity arrays. *Nano Energy*, 51, 400–407. DOI: 10.1016/j.nanoen.2018.06.083.

[3] Kim, T., Patil, S.S., Lee, K. (2022). Nanospace-confined worm-like $BiVO_4$ in TiO_2 space nanotubes (SPNTs) for photoelectrochemical hydrogen production. *Electrochimica Acta*, 432, 141213. DOI: 10.1016/j.electacta.2022.141213.

[4] Esmaili, H., Kowsari, E., Sarabadani Tafreshi, S., Ramakrishna, S., de Leeuw, N.H., Abdouss, M. (2022). TiO_2 nanoarrays modification by a novel Cobalt-heteroatom doped graphene complex for photoelectrochemical water splitting: An experimental and theoretical study. *Journal of Molecular Liquids*, 356, 118960. DOI: 10.1016/j.molliq.2022.118960.

[5] Han, M., Zhang, Z., Li, B., Hu, X., Wang, Z. (2022). Combined heterostructures between Bi_2S_3 nanosheets and H_2-treated TiO_2 nanorods for enhanced photoelectrochemical water splitting. *Applied Surface Science*, 598, 153850. DOI: 10.1016/j.apsusc.2022.153850.

[6] Zhou, T., Wang, J., Chen, S., Bai, J., Li, J., Zhang, Y., Li, L., Xia, L., Rahim, M., Xu, Q., Zhou, B. (2020). Bird-nest structured ZnO/TiO_2 as a direct Z-scheme photoanode with enhanced light harvesting and carriers kinetics for highly efficient and stable photoelectrochemical water splitting. *Applied Catalysis B: Environmental*, 267(800), 118599. DOI: 10.1016/j.apcatb.2020.118599.

[7] Li, J., McClure, J.P., Fu, R., Jiang, R., Chu, D. (2018). Understanding charge transfer dynamics in QDs-TiO_2 nanorod array photoanodes for solar fuel generation. *Applied Surface Science*, 429, 48–54. DOI: 10.1016/j.apsusc.2017.06.090.

[8] Moridon, S.N.F., Arifin, K., Yunus, R.M., Minggu, L.J., Kassim, M.B. (2022). Photocatalytic water splitting performance of TiO_2 sensitized by metal chalcogenides: A review. *Ceramics International*, 48(5), 5892–5907. DOI: 10.1016/j.ceramint.2021.11.199.

[9] Anaam, S.A.A., Saim, H., Sahdan, M.Z., Al-Gheethi, A. (2019). Defective TiO_2 with intrinsic point defects for photocatalytic hydrogen production: A review. *International Journal of Nanoelectronics and Materials*, 12(4), 495–516.

[10] Ahmad, A., Yerlikaya, G., Zia-ur-Rehman, Paksoy, H., Kardaş, G. (2020). Enhanced photoelectrochemical water splitting using gadolinium doped titanium dioxide nanorod array photoanodes. *International Journal of Hydrogen Energy*, 45(4), 2709–2719. DOI: 10.1016/j.ijhydene.2019.11.117.

[11] Li, T., Ding, D. (2020). Photoelectrochemical water splitting with black Ni/Si-doped TiO_2 nanostructures. *International Journal of Hydrogen Energy*, 45(41), 20983–20992. DOI: 10.1016/j.ijhydene.2020.05.182.

[12] Tong, M.-H., Wang, T.-M., Lin, S.-W., Chen, R., Jiang, X., Chen, Y.-X., Lu, C.-Z. (2023). Ultra-thin carbon doped TiO_2 nanotube arrays for enhanced visible-light photoelectrochemical water splitting. *Applied Surface Science*, 623, 156980. DOI: 10.1016/j.apsusc.2023.156980.

[13] Kumar, M.P., Jagannathan, R., Ravichandran, S. (2020). Photoelectrochemical System for Unassisted High-Efficiency Water-Splitting Reactions Using N-Doped TiO_2 Nanotubes. *Energy and Fuels*, 34(7), 9030–9036. DOI: 10.1021/acs.energyfuels.0c00634.

[14] Park, J., Lee, T.H., Kim, C., Lee, S.A., Choi, M.J., Kim, H., Yang, J.W., Lim, J., Jang, H.W. (2021). Hydrothermally obtained type-II heterojunction nanostructures of In_2S_3/TiO_2 for remarkably enhanced photoelectrochemical water splitting. *Applied Catalysis B: Environmental*, 295, 120276. DOI: 10.1016/j.apcatb.2021.120276.

[15] Lee, M.G., Yang, J.W., Park, H., Moon, C.W., Andoshe, D.M., Park, J., Moon, C.K., Lee, T.H., Choi, K.S., Cheon, W.S., Kim, J.J., Jang, H.W. (2022). Crystal Facet Engineering of TiO_2 Nanostructures for Enhancing Photoelectrochemical Water Splitting with $BiVO_4$ Nanodots. *Nano-Micro Letters*, 14(1), 1–15. DOI: 10.1007/s40820-022-00795-8.

[16] Sang, L., Ge, H., Sun, B. (2019). Probing plasmonic Ag nanoparticles on TiO_2 nanotube arrays electrode for efficient solar water splitting. *International Journal of Hydrogen Energy*, 44(30), 15787–15794. DOI: 10.1016/j.ijhydene.2018.09.094.

[17] Uyen, N.N., Thi, L., Tuyen, C., Hieu, L.T., Thu, T., Nguyen, T., Thao, H.P. (2022). TiO_2 Nanowires on TiO_2 Nanotubes Arrays (TNWs/TNAs) Decorated with Au Nanoparticles and Au Nanorods for Efficient PhotoelectrochemicalWater Splitting and Photocatalytic Degradation of Methylene Blue. *Coatings*, 12(12), 1957. DOI: 10.3390/coatings12121957

[18] Hou, X., Li, Z., Fan, L., Yuan, J., Lund, P.D., Li, Y. (2021). Effect of Ti foil size on the micro sizes of anodic TiO_2 nanotube array and photoelectrochemical water splitting performance. *Chemical Engineering Journal*, 425, 131415. DOI: 10.1016/j.cej.2021.131415.

[19] Chen, S., Li, C., Hou, Z. (2020). The novel behavior of photoelectrochemical property of annealing TiO_2 nanorod arrays. *Journal of Materials Science*, 55(14), 5969–5981. DOI: 10.1007/s10853-020-04379-y.

[20] Feng, T., Yam, F.K. (2023). The influence of hydrothermal treatment on TiO_2 nanostructure films transformed from titanates and their photoelectrochemical water splitting properties. *Surfaces and Interfaces*, 38, 102767. DOI: 10.1016/j.surfin.2023.102767.

[21] Yoon, D.H., Biswas, M.R.U.D., Sakthisabarimoorthi, A. (2022). Impact of crystalline core/amorphous shell structured black TiO_2 nanoparticles on photoelectrochemical water splitting. *Optical Materials*, 133, 113030. DOI: 10.1016/j.optmat.2022.113030.

[22] Joy, J., Mathew, J., George, S.C. (2018). Nanomaterials for photoelectrochemical water splitting – review. *International Journal of Hydrogen Energy*, 43(10), 4804–4817. DOI: 10.1016/j.ijhydene.2018.01.099.

[23] Zhao, H., Lei, Y. (2020). 3D Nanostructures for the Next Generation of High-Performance Nanodevices for Electrochemical Energy Conversion and Storage. *Advanced Energy Materials*, 10(28), 2001460. DOI: 10.1002/aenm.202001460.

[24] Lu, Y.W., Tseng, Y., Lee, J.S., Lee, W.J. (2016). Lateral-to-vertical growth transition of TiO_2 nanorods grown on FTO-glass substrate by hydrothermal process. *Digest Journal of Nanomaterials and Biostructures*, 11(2), 507–515.

[25] Ma, J., Ren, W., Zhao, J., Yang, H. (2016). Growth of TiO_2 nanoflowers photoanode for dye-sensitized solar cells. *Journal of Alloys and Compounds*, 692, 1004–1009. DOI: 10.1016/j.jallcom.2016.09.134.

[26] Desai, N.D., Khot, K.V., Dongale, T., Musselman, K.P., Bhosale, P.N. (2019). Development of dye sensitized TiO_2 thin films for efficient energy harvesting. *Journal of Alloys and Compounds*, 790, 1001–1013. DOI: 10.1016/j.jallcom.2019.03.246.

[27] Park, K.H., Dhayal, M. (2014). Simultaneous growth of rutile TiO_2 as 1D/3D nano-rod/nanoflower on FTO in one-step process enhances electrochemical response of photoanode in DSSC. *Electrochemistry Communications*, 49, 47–50. DOI: 10.1016/j.elecom.2014.09.011.

[28] Talib, A., Ahmad, M.K., Ahmad, N., Nafarizal, N., Mohamad, F., Soon, C.F., Suriani, A.B., Mamat, M.H., Murakami, K., Shimomura, M. (2020). Performance of dye-sensitized solar cell using size-controlled synthesis of TiO_2 nanostructure. *International Journal of Integrated Engineering*, 12(2), 106–114. DOI: 10.30880/ijie.2020.12.02.013.

[29] Norazlina, A., Mohamad, F., Talib, A., Ahmad, M.K., Nafarizal, N., Soon, C.F., Suriani, A.B., Mamat, M.H., Murakami, K., Shimomura, M. (2020). Fabrication rutile-phased TiO_2 film with different concentration of hydrochloric acid towards the performance of dye-sensitized solar cell. *International Journal of Integrated Engineering*, 12(2), 115–124. DOI: 10.30880/ijie.2020.12.02.014.

[30] Said, N.D.M., Sahdan, M.Z., Nayan, N., Saim, H., Adriyanto, F., Bakri, A.S., Morsin, M. (2018). Difference in structural and chemical properties of sol–gel spin coated Al doped TiO_2, Y doped TiO_2 and Gd doped TiO_2 based on trivalent dopants. *RSC Advances*, 8(52), 29686–29697. DOI: 10.1039/C8RA03950J.

[31] John, K.I., Adenle, A.A., Adeleye, A.T., Onyia, I.P., Amune-matthews, C., Omorogie, M.O. (2021). Unravelling the effect of crystal dislocation density and microstrain of titanium dioxide nanoparticles on tetracycline removal performance. *Chemical Physics Letters*, 776, 138725. DOI: 10.1016/j.cplett.2021.138725.

[32] Khot, A.C., Desai, N.D., Khot, K. V., Salunkhe, M.M., Chougule, M.A., Bhave, T.M., Kamat, R.K., Musselman, K.P., Dongale, T.D. (2018). Bipolar resistive switching and memristive properties of hydrothermally synthesized TiO_2 nanorod array: Effect of growth temperature. *Materials and Design*, 151, 37–47. DOI: 10.1016/j.matdes.2018.04.046.

[33] Dhandayuthapani, T., Sivakumar, R., Ilangovan, R. (2016). Growth of micro flower rutile TiO_2 films by chemical bath deposition technique: Study on the properties of structural, surface morphological, vibrational, optical and compositional. *Surfaces and Interfaces*, 4, 59–68. DOI: 10.1016/j.surfin.2016.09.006.

[34] Hassani, A., Faraji, M., Eghbali, P. (2020). Facile fabrication of mpg-C_3N_4/Ag/ZnO nanowires/Zn photocatalyst plates for photodegradation of dye pollutant. *Journal of Photochemistry and Photobiology A: Chemistry*, 400, 112665. DOI: 10.1016/j.jphotochem.2020.112665.

[35] Huang, H., Hou, X., Xiao, J., Zhao, L., Huang, Q., Chen, H., Li, Y. (2019). Effect of annealing atmosphere on the performance of TiO_2 nanorod arrays in photoelectrochemical water splitting. *Catalysis Today*, 330, 189–194. DOI: 10.1016/j.cattod.2018.04.011.

[36] Rahman, G., Joo, O.S. (2012). Photoelectrochemical water splitting at nanostructured α-Fe_2O_3 electrodes. *International Journal of Hydrogen Energy*, 37(19), 13989–13997. DOI: 10.1016/j.ijhydene.2012.07.037.

[37] Fàbrega, C., Andreu, T., Güell, F., Prades, J.D., Estradé, S., Rebled, J.M., Peiró, F., Morante, J.R. (2011). Effectiveness of nitrogen incorporation to enhance the photoelectrochemical activity of nanostructured TiO_2:NH_3 versus H_2-N_2 annealing. *Nanotechnology*, 22(23), 1–7. DOI: 10.1088/0957-4484/22/23/235403.

[38] Issar, S., Poddar, P., Mehra, N.C., Mahapatro, A.K. (2017). Growth of flower-like patterns of TiO_2 nanorods over FTO substrate. *Integrated Ferroelectrics*, 184(1), 166–171. DOI: 10.1080/10584587.2017.1368640.

[39] Shao, Y., Tang, D., Sun, J., Lee, Y., Xiong, W. (2004). Lattice deformation and phase transformation from nano-scale anatase to nano-scale rutile TiO_2 prepared by a sol-gel technique. *China Particuology*, 2(3), 119–123. DOI: 10.1016/s1672-2515(07)60036-0.

[40] Lu, X., Gao, S., Wu, P., Zhang, Z., Zhang, L., Li, X., Qin, X. (2023). In Situ High-Pressure Raman Spectroscopic, Single-Crystal X-ray Diffraction, and FTIR Investigations of Rutile and TiO_2II. *Minerals*, 13(5), 703. DOI: 10.3390/min13050703.

[41] Mayabadi, A.H., Waman, V.S., Kamble, M.M., Ghosh, S.S., Gabhale, B.B., Rondiya, S.R., Rokade, A.V., Khadtare, S.S., Sathe, V.G., Pathan, H.M., Gosavi, S.W., Jadkar, S.R. (2014). Evolution of structural and optical properties of rutile TiO_2 thin films synthesized at room temperature by chemical bath deposition method. *Journal of Physics and Chemistry of Solids*, 75(2), 182–187. DOI: 10.1016/j.jpcs.2013.09.008.

[42] Wang, S., Zhang, J., Smyth, J.R., Zhang, J., Liu, D., Zhu, X., Wang, X., Ye, Y. (2020). Crystal Structure, Thermal Expansivity and High-Temperature Vibrational Spectra on Natural Hydrous Rutile. *Journal of Earth Science*, 31(6), 1190–1199. DOI: 10.1007/s12583-020-1351-5.

[43] Rathore, N., Kulshreshtha, A., Shukla, R.K., Sharma, D. (2021). Optical, structural and morphological properties of Fe substituted rutile phase TiO_2 nanoparticles. *Physica B: Condensed Matter*, 600, 412609. DOI: 10.1016/j.physb.2020.412609.

[44] Ben Naceur, J., Jrad, F., Souiwa, K., Ben Rhouma, F., Chtourou, R. (2021). Hydrothermal reaction time effect in wettability and photoelectrochemical properties of TiO_2 nanorods arrays films. *Optik*, 239, 166794. DOI: 10.1016/j.ijleo.2021.166794.

[45] Wu, W., Hong, M., Guo, X., Guo, J., Jiang, X. (2016). An approach toward TiO_2 nanostructure growth with tunable properties: influence of concentration of titanium butoxide in a hydrothermal process. *Journal of Materials Science: Materials in Electronics*, 27(7), 7049–7054. DOI: 10.1007/s10854-016-4662-7.

[46] Nguyen, M.H., Kim, K.S. (2021). Analysis on growth mechanism of TiO_2 nanorod structures on FTO glass in hydrothermal process. *Journal of Industrial and Engineering Chemistry*, 104, 445–457. DOI: 10.1016/j.jiec.2021.08.045.

[47] Ali, W., Jaffari, G.H., Khan, S., Liu, Y. (2018). Morphological control of 1D and 3D TiO_2 nanostructures with ammonium hydroxide and TiO_2 compact layer on FTO coated glass in hydrothermal synthesis. *Materials Chemistry and Physics*, 214, 48–55. DOI: 10.1016/j.matchemphys.2018.04.081.

[48] Musa, M.Z., Mamat, M.H., Vasimalai, N., Shameem Banu, I.B., Malek, M.F., Ahmad, M.K., Suriani, A.B., Mohamed, A., Rusop, M. (2020). Fabrication and structural properties of flower-like TiO_2 nanorod array films grown on glass substrate without FTO layer. *Materials Letters*, 273, 127902. DOI: 10.1016/j.matlet.2020.127902.

[49] Jordan, V., Javornik, U., Plavec, J., Podgornik, A., Rečnik, A. (2016). Self-assembly of multilevel branched rutile-type TiO_2 structures via oriented lateral and twin attachment. *Scientific Reports*, 6, 1–13. DOI: 10.1038/srep24216.

[50] Liu, B., Aydil, E.S. (2009). Growth of oriented single-crystalline rutile TiO_2 nanorods on transparent conducting substrates for dye-sensitized solar cells. *Journal of the American Chemical Society*, 131(11), 3985–3990. DOI: 10.1021/ja8078972.

[51] Burungale, V.V., Satale, V.V., More, A.J., Sharma, K.K.K., Kamble, A.S., Kim, J.H., Patil, P.S. (2016). Studies on effect of temperature on synthesis of hierarchical TiO_2 nanostructures by surfactant free single step hydrothermal route and its photoelectrochemical characterizations. *Journal of Colloid and Interface Science*, 470, 108–116. DOI: 10.1016/j.jcis.2016.02.026.

[52] Wang, X., Xiao, Y., Zeng, D., Xie, C. (2015). Optimizing the packing density of TiO_2 nanorod arrays for enhanced light harvesting by a light trapping effect and its photocatalytic decomposition of gaseous benzene. *CrystEngComm*, 17(5), 1151–1158. DOI: 10.1039/c4ce02129k.

[53] Lin, J., Heo, Y.U., Nattestad, A., Sun, Z., Wang, L., Kim, J.H., Dou, S.X. (2014). 3D hierarchical rutile TiO_2 and metal-free organic sensitizer producing dye-sensitized solar cells 8.6% conversion efficiency. *Scientific Reports*, 4, 1–8. DOI: 10.1038/srep05769.

[54] Maria, A.S.M., Kumaresan, N., Ramamurthi, K., Sethuraman, K., Moorthy, B.S., Ramesh, B.R., Ganesh, V. (2018). Influence of heat treatment on the properties of hydrothermally grown 3D/1D TiO_2 hierarchical hybrid microarchitectures over TiO_2 seeded FTO substrates. *Applied Surface Science*, 449, 122–131. DOI: 10.1016/j.apsusc.2018.01.122

[55] Song, Z., Zhou, H., Tao, P., Wang, B., Mei, J., Wang, H. (2016). The synthesis of TiO_2 nano flowers and their application in electron field emission and self-powered ultraviolet photodetector. *Materials Letters*, 180, 179–183. DOI: 10.1016/j.matlet.2016.05.178.

[56] Ye, M., Liu, H.Y., Lin, C., Lin, Z. (2013). Hierarchical rutile TiO_2 flower cluster-based high efficiency dye-sensitized solar cells via direct hydrothermal growth on conducting substrates. *Small*, 9(2), 312–321. DOI: 10.1002/smll.201201590.

[57] Faisal, A.Q.D. (2014). Synthesis and characteristics study of TiO_2 nanowires and nanoflowers on FTO/glass and glass substrates via hydrothermal technique. *Journal of Materials Science: Materials in Electronics*, 26(1), 317–321. DOI: 10.1007/s10854-014-2402-4.

[58] Issar, S., Mahapatro, A.K. (2019). Hydrothermally grown rutile titanium dioxide nanostructures with various morphologies. *Materials Science in Semiconductor Processing*, 104, 104676. DOI: 10.1016/j.mssp.2019.104676.

[59] Khizir, H.A., Abbas, T.A.H. (2021). Hydrothermal growth and controllable synthesis of flower-shaped TiO_2 nanorods on FTO coated glass. *Journal of Sol-Gel Science and Technology*, 98(3), 487–496. DOI: 10.1007/s10971-021-05531-z.

[60] Lu, S., Yang, S., Hu, X., Liang, Z., Guo, Y., Xue, Y., Cui, H., Tian, J. (2019). Fabrication of TiO_2 nanoflowers with bronze (TiO_2(B))/anatase heterophase junctions for efficient photocatalytic hydrogen production. *International Journal of Hydrogen Energy*, 44(45), 24398–24406. DOI: 10.1016/j.ijhydene.2019.07.212.

[61] He, Z., Cai, Q., Fang, H., Situ, G., Qiu, J., Song, S., Chen, J. (2013). Photocatalytic activity of TiO_2 containing anatase nanoparticles and rutile nanoflower structure consisting of nanorods. *Journal of Environmental Sciences (China)*, 25(12), 2460–2468. DOI: 10.1016/S1001-0742(12)60318-0.

[62] Ramli, N.F., Fahsyar, P.N.A., Ludin, N.A., Teridi, M.A.M., Ibrahim, M.A., Zaidi, S.H., Sepeai, S. (2019). Compatibility between compact and mesoporous TiO_2 layers on the optimization of photocurrent density in photoelectrochemical cells. *Surfaces and Interfaces*, 17, 100341. DOI: 10.1016/j.surfin.2019.100341.

[63] Wategaonkar, Sandeep B., Vinayak G. Parale, Sawanta S. Mali, Chang-Kook Hong, Rani P. Pawar, Parvejha S. Maldar, Annasaheb V. Moholkar, Hyung-Ho Park, Balasaheb M. Sargar, R.K.M. (2021). Influence of Tin Doped TiO_2 Nanorods on Dye Sensitized Solar Cells. *Materials*, 14 (21), 6282. DOI: 10.3390/ma14216282

[64] Ni, S., Guo, F., Wang, D., Jiao, S., Wang, J., Zhang, Y., Wang, B., Feng, P., Zhao, L. (2019). Modification of TiO_2 nanowire arrays with sn doping as photoanode for highly efficient dye-sensitized solar cells. *Crystals*, 9(2) DOI: 10.3390/cryst9020113.

[65] Dai, G., Liu, S., Liang, Y., Luo, T. (2013). Synthesis and enhanced photoelectrocatalytic activity of p-n junction Co_3O_4 /TiO_2 nanotube arrays. *Applied Surface Science*, 264, 157–161. DOI: 10.1016/j.apsusc.2012.09.160.

[66] Yu, J., Wang, B. (2010). Effect of calcination temperature on morphology and photoelectrochemical properties of anodized titanium dioxide nanotube arrays. *Applied Catalysis B: Environmental*, 94(3–4), 295–302. DOI: 10.1016/j.apcatb.2009.12.003.

[67] Arifin, K., Yunus, R.M., Minggu, L.J., Kassim, M.B. (2021). Improvement of TiO_2 nanotubes for photoelectrochemical water splitting: Review. *International Journal of Hydrogen Energy*, 46(7), 4998–5024. DOI: 10.1016/j.ijhydene.2020.11.063.

[68] Jeong, H.W., Haihua, W., Samu, G.F., Rouster, P., Szilágyi, I., Park, H., Janáky, C. (2021). The effect of nanostructure dimensionality on the photoelectrochemical properties of derived TiO_2 films. *Electrochimica Acta*, 373, 137900. DOI: 10.1016/j.electacta.2021.137900.

[69] Huang, X., Zhang, R., Gao, X., Yu, B., Gao, Y., Han, Z. gang (2021). TiO_2-rutile/anatase homojunction with enhanced charge separation for photoelectrochemical water splitting. *International Journal of Hydrogen Energy*, 46(52), 26358–26366. DOI: 10.1016/j.ijhydene.2021.05.118.

[70] Fang, Y., Hodgson, R., Lee, W.C., Le, H., Chan, H.W.B., Hassan, H.M., Alsohaimi, I.H., Canciani, G.E., Qian, R., Chen, Q. (2023). Light trapping by porous TiO_2 hollow hemispheres for high efficiency photoelectrochemical water splitting. *Physical Chemistry Chemical Physics*, 25(16), 11253–11260. DOI: 10.1039/d2cp04246k.

[71] Habibi-Hagh, F., Jafari Foruzin, L., Nasirpouri, F. (2022). Remarkable improvement of photoelectrochemical water splitting in pristine and black anodic TiO_2 nanotubes by enhancing microstructural ordering and uniformity. *International Journal of Hydrogen Energy*, 48(30), 11225–11236. DOI: 10.1016/j.ijhydene.2022.07.158.